

Localized stationary and traveling reaction-diffusion patterns in a two-layer $A + B \rightarrow$ oscillator system

M. A. Budroni*

Department of Chemistry and Pharmacy, University of Sassari, Via Vienna 2, Sassari 07100, Italy

A. De Wit†

Université libre de Bruxelles (ULB), Nonlinear Physical Chemistry Unit, Faculté des Sciences, CP231, 1050 Brussels, Belgium

(Received 20 December 2015; revised manuscript received 8 April 2016; published 9 June 2016)

When two solutions containing separate reactants A and B of an oscillating reaction are put in contact in a gel, localized spatiotemporal patterns can develop around the contact zone thanks to the interplay of reaction and diffusion processes. Using the Brusselator model, we explore analytically the deployment in space and time of the bifurcation diagram of such an $A + B \rightarrow$ oscillator system. We provide a parametric classification of possible instabilities as a function of the ratio of the initial reactant concentrations and of the reaction intermediate species diffusion coefficients. Related one-dimensional reaction-diffusion dynamics are studied numerically. We find that the system can spatially localize waves and Turing patterns as well as induce more complex dynamics such as *zigzag* spatiotemporal waves when Hopf and Turing modes interact.

DOI: [10.1103/PhysRevE.93.062207](https://doi.org/10.1103/PhysRevE.93.062207)

I. INTRODUCTION

Propagation of localized reaction zones can be obtained when initially separated reactants A and B meet by diffusion and start to react. In the case of simple $A + B \rightarrow C$ reactions, the properties of the related reaction-diffusion (RD) fronts have been well characterized [1]. In gels, these fronts are known to travel at a speed and in a direction that depend on the ratio of initial reactant concentrations and diffusion coefficients [2]. In absence of a gel, convective dynamics due to buoyancy effects [3,4] or viscosity-driven [5,6] instabilities have been shown to provide new reaction-diffusion-convection (RDC) patterns. There is currently also interest in understanding the properties of such localized reaction zones in the case of autocatalytic reactions [7]. RDC dynamics for which localized traveling waves couple to buoyancy-driven fingering phenomena have been indeed characterized when two solutions each containing a subpart of the oscillating Belousov-Zhabotinsky (BZ) [8,9] reaction are put in contact in the gravity field [7]. In order to understand the properties of these RDC patterns, there is a need to first decipher the spatiotemporal properties of the underlying autocatalytic RD fronts.

Localized autocatalytic RD structures have long been studied in the presence of gradients in the concentrations of given reactants [10,11]. In experiments, these localized patterns emerge typically in a piece of gel fed from two lateral sides with different reactants [so-called continuously fed unstirred reactors (CFUR)]. Initially, the gel contains no reactant and dissipative spatiotemporal dynamics develop in the central part of the gel once the reactants meet by diffusion. Either localized waves (such as excyclons for instance [12,13]) or Turing patterns spatially confined in a part of the reactor [14–18] are then obtained experimentally depending on which

instability is controlling the system. From a theoretical point of view, several works have already characterized the properties of RD patterns localized by ramps of concentrations of the main reactants maintained by the feeding of the system from the sides [10,11,16–24]. These concentration gradients can lead to coexistence in different parts of the reactor of waves and Turing patterns or to composite stationary spatial structures [17,23–28]. Some analysis of this problem has been performed with the classical Brusselator model [11,29,30] to investigate the impact of nonuniform spatial distributions of one initial reactant while the other is set homogeneously and works as a bifurcation parameter. Typically, the concentration profile of the nonuniform reactant is considered with a minimum in the central zone of the reactor. It was reported numerically that the system dynamics can switch from localized steady structures to propagating chemical waves as a function of the relative values of the initial reactant concentrations and diffusion coefficients [10,11]. Deeper insights on the resulting RD patterns, such as parametric conditions for the onset of the instabilities, amplitude and wavelength, were obtained analytically by means of a linear stability analysis [19,20].

Other localized RD structures like, for instance, a Turing pattern localized in an oscillating background (or vice-versa) can be obtained with homogeneous feeding of the reactants in the vicinity of a codimension-two Turing-Hopf (CTH) point, i.e., conditions for which the thresholds of the Turing and Hopf instabilities coincide [17,27,28,31–39]. Similarly, several types of complex behavior, including spatiotemporal chaos induced by the interplay between Turing and Hopf domains, have been predicted [40,41]. Finally, cross-diffusion has been also shown to drive the formation of localized reaction-diffusion patterns and their interaction with propagating waves [42–46].

The situation that has not received as much attention yet is the $A + B \rightarrow$ oscillator case, in which two gels, each of them containing different reactants A or B of an oscillatory reaction, are put in contact in a closed reactor. Each part of this system is unable initially to yield any RD pattern as it

*mabudroni@uniss.it; <http://physchem.uniss.it/cnl.dyn/budroni.html>

html

†adewit@ulb.ac.be

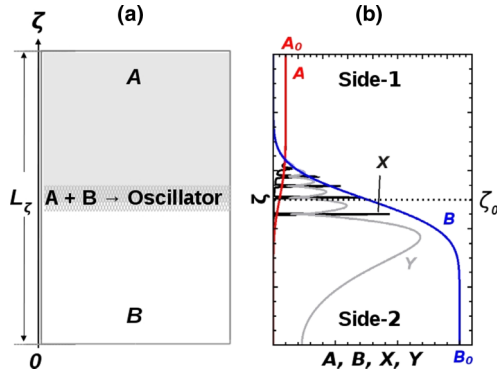


FIG. 1. (a) Sketch of the two-layer configuration under analysis, where two pieces of gels, each of them containing different reactants of an oscillatory reaction, are put in contact; (b) spatial profiles of the Brusselator chemical species (A, B, X, Y) some time after putting regions 1 and 2 in contact when reactant consumption can be neglected.

contains only A or B that cannot give any nonlinear dynamics alone. Yet, once the gels are in contact, the reactants can diffuse and start to provide locally all species needed for the complex chemical processes to start. This problem is the generalization of a simple $A + B \rightarrow C$ front case to $A + B \rightarrow$ oscillatory and excitable kinetics, much less characterized.

In this context, we have recently initiated the study of such $A + B \rightarrow$ oscillator systems with the BZ reaction [47], in which the oscillatory mechanism is active in the reaction zone between two initially spatially separated pools of BZ reactants slowly diffusing one into the other [as sketched in Fig. 1(a)]. Thanks to a combined experimental and numerical approach, it has been shown how the two-layer configuration associated with the nonlinear chemical kinetics is a convenient means to induce self-sustained localized patterns and is a rich source of complex dynamics [47]. Composite traveling structures result from the interaction between chemical fronts and localized waves, and the transition between different spatiotemporal behaviors can be directly controlled by varying the initial concentration of the organic substrate of the BZ medium layered on one side, which affects the local excitability. The complexity of the BZ oscillator calls for simpler model systems through which spatiotemporal RD structures obtained with the two-layer configuration can be theoretically analyzed and classified.

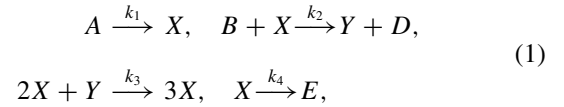
To this end, we use here the Brusselator model, on which both dynamical and stationary instabilities can be explored and analytical progresses can be made [10,11,20,24,31,48,49]. We provide a first insight into the possible dynamics and coexistence of different instability modes in an $A + B \rightarrow$ oscillator system. We show analytically that, depending upon the ratio of the initial concentration of the two reactants and the ratio of diffusion coefficients of the reaction intermediates, the system can exhibit either localized waves, localized stationary Turing structures, or a combination of both modes expanding in space around a codimension-two Turing-Hopf (CTH) point. We study numerically the spatiotemporal properties of these RD patterns in the case of a one-dimensional system. This analysis provides a theoretical basis to develop experiments

studying localized RD patterns using oscillating reactions in gels or RDC dynamics with the same reactants put in contact in reactors in the presence of hydrodynamic instabilities.

The article is organized as follows: in Sec. II, we describe the Brusselator model with the specific initial and boundary conditions akin to obtain structures in a localized reaction zone upon contact along a given interface between two solutions each containing a different initial reactant of the chemical oscillator. In Sec. III, we derive analytically the conditions to obtain spatially localized Hopf, localized Turing, or a CTH bifurcation. In particular, we study analytical spatiotemporal bifurcation diagrams to be expected as a function of the relative diffusivity and concentration of chemical species, culminating in a general classification of the possible instability scenarios, which can be obtained in this relevant parameter space. Section IV presents results of numerical simulations of the RD model in one dimension before a concluding discussion (Sec. V) is drawn.

II. RD EQUATIONS

The kinetic scheme of the irreversible Brusselator model reads [11,29,30]



where $\{A, B\}$ are the initial reactants and $\{X, Y\}$ are the reaction intermediates, featuring the autocatalytic (X) and the inhibitor (Y) species, respectively. $\{k_i, i = 1, 4\}$ represents the set of rate constants. Here, we study a two-layer configuration in which the pools of reactants A and B are initially separated at $\zeta = \zeta_0$ along the spatial domain of length L_ζ (see Fig. 1). There is initially no intermediate species X and Y such that the initial condition reads

$$\begin{aligned} (A, B, X, Y) &= (A_0, 0, 0, 0) \text{ (side 1) for } \zeta > \zeta_0 = L_\zeta/2, \\ (A, B, X, Y) &= (0, B_0, 0, 0) \text{ (side 2) for } \zeta \leq \zeta_0 = L_\zeta/2. \end{aligned} \quad (2)$$

The formation of the intermediates X and Y occurs upon diffusive mixing and reaction between the two reactants (or more generally reactant pools) A and B across the initial contact line localized at $\zeta_0 = L_\zeta/2$ [see Fig 1(b)].

No-flux boundary conditions are considered for all species at the borders $\zeta = 0$ and $\zeta = L_\zeta$. For simplicity, we consider that the main reactants present similar diffusivity $D_a \sim D_b = D$. Following a standard scaling of the variables (see Refs. [21,30,50]), the reaction-diffusion (RD) equations of the irreversible Brusselator read

$$\partial_t A = D \nabla^2 A - k_a A, \quad (3)$$

$$\partial_t B = D \nabla^2 B - k_b B X, \quad (4)$$

$$\partial_t X = D_x \nabla^2 X + A - (B + 1)X + X^2 Y, \quad (5)$$

$$\partial_t Y = D_y \nabla^2 Y + B X - X^2 Y, \quad (6)$$

with $k_a = k_1/k_4$ and $k_b = k_2/\sqrt{k_3 k_4}$ [50]. In a closed system, our out-of-equilibrium description requires that the initial concentrations A_0 and B_0 of the reactants are much larger than the intermediate concentrations and that they are slowly consumed (so-called *pool chemical approximation*) as compared to the

timescale characterizing the RD dynamics of the intermediate species, so that they change mainly because of diffusion. In the model Eqs. (3)–(6), the rate of reactant depletion can be controlled by means of the kinetic parameters k_a and k_b .

The pool chemical hypothesis, enabling us to neglect equilibria and reactant consumption, holds as long as the system maintains far-from-equilibrium conditions and, referring to the definition of k_a and k_b , it successfully applies to the Brusselator when $k_1 \ll k_4$ and $k_2 \ll \sqrt{k_3 k_4}$ (in other terms, when the autocatalytic process and the consumption of the autocatalytic species are faster than the reactant depletion steps). This condition is physically possible in chemical oscillators and is particularly reliable with the Belousov-Zhabotinsky system, able to maintain oscillations and RD structures in quasistationary conditions quite a long time in batch reactors before evolving to equilibrium. For the BZ system, we have recently shown that numerical simulations of an analogous two-layer system carried out by using the Oregonator model without reactants consumption compare favorably with the spatiotemporal dynamics found in corresponding experiments [47]. On the basis of this evidence, we assume here that $k_a = k_b = 0$, which greatly simplifies the complexity of the problem and allows us to develop analytical progresses.

In a homogeneous system with constant concentration A_0 and B_0 in space and time, Eqs. (5) and (6) admit the homogeneous steady state (SS) $(X_{ss}, Y_{ss}) = (A_0, B_0/A_0)$. If B_0 is chosen as the bifurcation parameter, this SS may become unstable toward a Hopf instability if $B_0 > B_c^H = 1 + A_0^2$, evolving then into a homogeneous limit cycle characterized by a critical frequency $\omega = iA_0$. In the presence of differential diffusion, this SS can become unstable toward a Turing instability when $B_0 > B_c^T = (1 + A_0\sqrt{\delta})^2$, where $\delta = D_x/D_y$. A stationary spatial pattern emerges then characterized by an intrinsic critical wave vector $k_c^2 = A_0/\sqrt{D_x D_y}$. The thresholds of these two instabilities coincide at the Turing-Hopf codimension-two (CTH) point such that $B_c = B_c^H = B_c^T$. In a homogeneous system, the CTH is obtained for the critical ratio of diffusion coefficients $\delta_c = [(\sqrt{1 + A_0^2} - 1)/A_0]^2$. A characterization of the instability regions of the homogeneous system is given for $A_0 = 1$ in the parameter space (δ, B_0) shown below [Fig. 4(a)].

Our objective here is to analyze how these instability thresholds develop in space and time when the profiles of reactant concentrations $A(\zeta, t)$ and $B(\zeta, t)$ are themselves evolving dynamically when controlled by a diffusive process. This characterization is then correlated to the phenomenology observed from numerical simulations of the RD Eqs. (3)–(6). The validity of our analytical predictions obtained without reactant consumption ($k_a = k_b = 0$) are finally discussed in regard to the simulations of the full Eqs. (3)–(6) with nonzero values of the kinetic parameters k_a and k_b .

III. SPATIOTEMPORAL BIFURCATION DIAGRAMS AND PARAMETRIC CLASSIFICATION

Analytical solutions to the diffusive Eqs. (3) and (4) starting from the initial conditions Eq. (2) with no-flux boundary

conditions and $k_a = k_b = 0$ are [51]

$$A(\zeta, t) = \frac{A_0}{2} \operatorname{erfc}\left(-\frac{(\zeta - \zeta_0)}{\sqrt{4Dt}}\right), \quad (7)$$

$$B(\zeta, t) = \frac{B_0}{2} \operatorname{erfc}\left(\frac{(\zeta - \zeta_0)}{\sqrt{4Dt}}\right). \quad (8)$$

As the consumption of the initial reactants is neglected, the different role played by species A and B results from their different initial distributions Eq. (2).

As a consequence of Eqs. (7) and (8), the critical value of the control parameter B_0 above which the system becomes unstable toward a Hopf bifurcation also evolves as a function of space and time as

$$H(\zeta, t) = 1 + A^2(\zeta, t) = 1 + \left[\frac{A_0}{2} \operatorname{erfc}\left(-\frac{(\zeta - \zeta_0)}{\sqrt{4Dt}}\right)\right]^2. \quad (9)$$

Similarly, the critical curve above which a Turing instability sets in writes

$$T(\zeta, t) = [1 + \sqrt{\delta}A(\zeta, t)]^2 = \left[1 + \frac{\sqrt{\delta}A_0}{2} \operatorname{erfc}\left(-\frac{(\zeta - \zeta_0)}{\sqrt{4Dt}}\right)\right]^2. \quad (10)$$

An illustration of how the stability of the system changes in space in response to the spatial distribution of the main reactants is sketched in Fig. 2 for a given time, t . The lower curve [either $H(\zeta, t)$ or $T(\zeta, t)$] indicates which instability is locally governing the system dynamics, provided that it also lies below the concentration profile $B(\zeta, t)$. For instance, by following from top to bottom the downward increasing curve $B(\zeta, t)$, we observe stationary states for $\zeta > \zeta_T$, where $B(\zeta, t) < T(\zeta, t) < H(\zeta, t)$. The system becomes unstable to a Turing instability for $\zeta_{CTH} < \zeta < \zeta_T$, where $T(\zeta, t) < B(\zeta, t) < H(\zeta, t)$. For $\zeta < \zeta_{CTH}$, $H(\zeta, t) < T(\zeta, t) < B(\zeta, t)$ and the Hopf instability locally controls the dynamics.

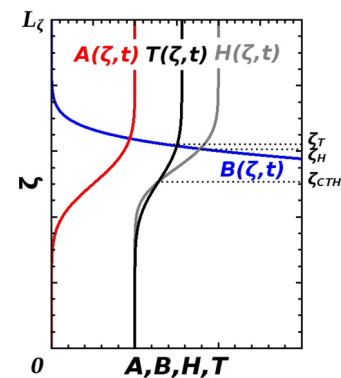


FIG. 2. Schematic of spatially dependent concentration profiles, $A(\zeta, t)$ (red), $B(\zeta, t)$ (blue), and critical thresholds, $H(\zeta, t)$ (gray) and $T(\zeta, t)$ (black), at a given time t . In this view $B(\zeta, t)$ goes out of scale. ζ_{CTH} locates the codimension-two point, where $H(\zeta, t)$ intersects $T(\zeta, t)$, while ζ_H and ζ_T identify the intersection points of $B(\zeta, t)$ with $H(\zeta, t)$ and $T(\zeta, t)$, respectively.

In general, the Hopf instability controls the regions of the spatial coordinate where

$$\begin{aligned} H(\zeta, t) &< B(\zeta, t) \\ H(\zeta, t) &< T(\zeta, t), \end{aligned}$$

while Turing structures can develop where the following conditions are met simultaneously

$$\begin{aligned} T(\zeta, t) &< B(\zeta, t) \\ T(\zeta, t) &< H(\zeta, t). \end{aligned}$$

The points where the instability profiles cross each other and intersect $B(\zeta, t)$ define important references for mapping the spatiotemporal deployment of the different regimes. The location $\zeta_{\text{CTH}}(t)$ of the codimension-two point, where $H(\zeta, t) = T(\zeta, t)$, permits us to separate the domains in which one instability prevails on the other. This border point is found to evolve as

$$\begin{aligned} \zeta_{\text{CTH}}(t) - \zeta_0 &= -\text{erf}^{-1} \left[1 - \frac{4\sqrt{\delta}}{(1-\delta)A_0} \right] \sqrt{4Dt}, \\ \text{with } A_0 > 0 \text{ and } \sqrt{\delta} &\in \left(0, \frac{\sqrt{1+A_0^2}-1}{A_0} \right). \end{aligned} \quad (11)$$

The Hopf regime dominates the Turing one [i.e., $H(\zeta, t) < T(\zeta, t)$] in the spatial domain, where

$$\zeta < \zeta_{\text{CTH}}(t). \quad (12)$$

For δ values beyond the constraints given in Eq. (11), no intersection is possible and the Hopf threshold lies below $T(\zeta, t)$. Also, note that $\zeta_{\text{CTH}}(t)$ depends explicitly on A_0 and δ , while it is independent of B_0 .

A dependence in B_0 is found by solving the inequality $H(\zeta, t) < B(\zeta, t)$, from which we obtain that the system is also locally in the Hopf regime when

$$\zeta < \zeta_H(t), \quad (13)$$

where

$$\begin{aligned} \zeta_H(t) - \zeta_0 &= -\text{erf}^{-1} \left(\frac{B_0 + A_0^2 - \sqrt{B_0^2 - 4A_0^2(1-B_0)}}{A_0^2} \right) \\ &\times \sqrt{4Dt} \quad \forall \quad A_0 > 0, B_0 \geq 1. \end{aligned}$$

According to Eqs. (12) and (13), the system can destabilize into Hopf modes either for

$$\zeta < \zeta_H(t) < \zeta_{\text{CTH}}(t) \quad (14)$$

or

$$\zeta < \zeta_{\text{CTH}}(t) < \zeta_H(t). \quad (15)$$

As discussed below, the former condition [Eq. (14)] holds when the Hopf instability can only develop while the latter [Eq. (15)] is operational in the presence of both instabilities along the system.

By taking into account condition $T(\zeta, t) < B(\zeta, t)$ combined to Eq. (12), the spatiotemporal evolution of the Turing

regime can be isolated by

$$\zeta_{\text{CTH}}(t) < \zeta(t) < \zeta_T(t), \quad (16)$$

where

$$\begin{aligned} \zeta_T(t) - \zeta_0 &= -\text{erf}^{-1} \\ &\times \left\{ \frac{B_0 + 2\sqrt{\delta}A_0 + \delta A_0^2 - \sqrt{B_0[B_0 + 4\sqrt{\delta}A_0(1 + \sqrt{\delta}A_0)]}}{\delta A_0^2} \right\} \\ &\times \sqrt{4Dt} \end{aligned} \quad (17)$$

provided $A_0 > 0$, $B_0 \geq 1$, and $\sqrt{\delta} \in (0, \frac{\sqrt{1+A_0^2}-1}{A_0})$.

Due to geometrical constraints, the intersection $\zeta_{\text{CTH}}(t)$ between the profiles $T(\zeta, t)$ and $H(\zeta, t)$ can solely precede or follow the position of points $\zeta_H(t)$ and $\zeta_T(t) \forall t$. Together with condition Eq. (12), this fact implies that the relative evolution of these critical thresholds follows either

$$\zeta_T(t) < \zeta_H(t) < \zeta_{\text{CTH}}(t) \quad \forall t \quad (18)$$

[see Fig. 3(a)] or

$$\zeta_{\text{CTH}}(t) < \zeta_H(t) < \zeta_T(t) \quad \forall t, \quad (19)$$

as shown in Fig. 3(b).

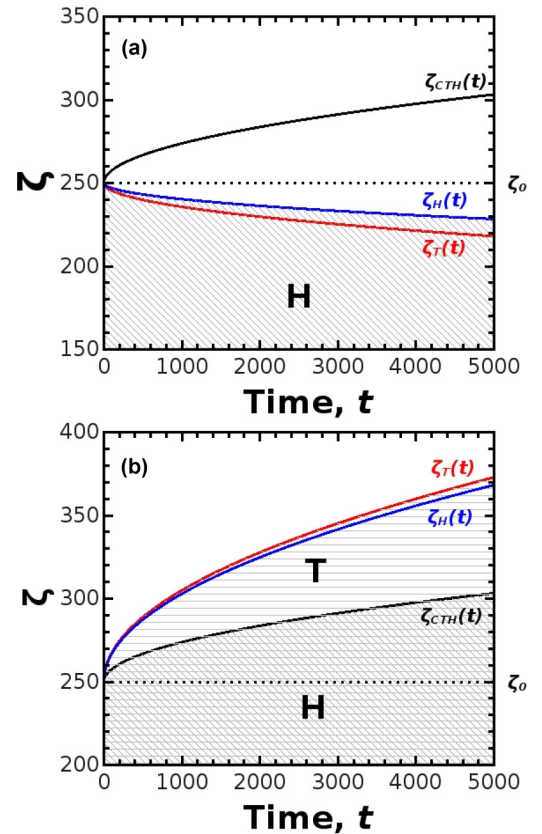


FIG. 3. Spatiotemporal bifurcation diagrams showing the evolution of the critical points $\zeta_{\text{CTH}}(t)$, $\zeta_H(t)$, and $\zeta_T(t)$ for the two typical situations of our problem, when the reactant consumption is neglected. $A_0 = 1$, $D = D_x = 1$, $\delta = 0.1$, $k_a = k_b = 0$, and (a) $B_0 = 2$, only the Hopf instability can locally develop, (b) $B_0 = 15$, both the Turing and Hopf instability coexist.

Equations (18) and (19) are the relevant conditions for localizing the instability domains and describing the spatiotemporal development in these two possible scenarios. They are analyzed graphically in Fig. 3, where we compare $\zeta_{\text{CTH}}(t)$, $\zeta_H(t)$, and $\zeta_T(t)$. Figure 3(a) illustrates the case where only the Hopf instability can locally set in [Eq. (18)], while in the second example [Fig. 3(b)], the Turing instability is also at play [Eq. (19)]. In Fig. 3(a), we observe that $\zeta_T(t)$ (red curve) is strictly lower than $\zeta_{\text{CTH}}(t)$ (black curve), hindering the possibility of satisfying condition Eq. (16) for the existence of a Turing-controlled domain. Bearing in mind the illustrative Fig. 2, it can be realized that, in the region $\zeta < \zeta_{\text{CTH}}(t)$, the Turing threshold $T(\zeta, t)$ lies always beyond $H(\zeta, t)$ [$H(\zeta, t) < T(\zeta, t)$] and the Hopf instability thus dominates exclusively the system dynamics as soon as $B(\zeta, t) > H(\zeta, t)$. Indeed, the Hopf domain extends for $\zeta < \zeta_H(t)$ (blue curve) consistently with condition Eq. (14). Notice that, in our problem, it is not possible to find any analog to this situation with Turing modes exclusively active.

Figure 3(b) shows that $\zeta_T(t) > \zeta_{\text{CTH}}(t)$ at all times and the spatial region embedded between these two trends is unstable toward a Turing instability. $\zeta_H(t)$ lies within this region and the Hopf instability can thus prevail only below $\zeta_{\text{CTH}}(t)$, according to condition Eq. (15).

Thanks to relation Eqs. (13)–(17) and corresponding parametric constraints, we can also derive the conditions (independent of time and space), in which these possible instability scenarios can develop, as a function of δ and B_0 , for a given A_0 . In particular, Eqs. (16) and (17) allow us to predict where Hopf and Turing instabilities can separately coexist over the spatial domain. From the comparison between the members of Eq. (16), it follows that $\zeta_{\text{CTH}}(t) < \zeta_T(t)$, which, since the inverse error functions, $-\text{erf}^{-1}()$, are monotonically decreasing in the domain $(-1, 1)$, is satisfied when their arguments obey

$$\frac{1 - \delta A_0 - 4\sqrt{\delta} A_0}{1 - \delta} > \frac{(2\sqrt{\delta} A_0 + B_0) - \sqrt{B_0(B_0 + 4\sqrt{\delta} A_0 + 4\delta A_0^2)}}{\delta A_0}. \quad (20)$$

This leads to

$$B_0 > \frac{A_0(\delta + 1)^2}{(\delta - 1)[2\sqrt{\delta} + A_0(\delta - 1)]} \quad (21)$$

$$\forall \delta < \left(\frac{\sqrt{1 + A_0^2} - 1}{A_0} \right)^2 \text{ and } A_0 > 0.$$

Starting from condition Eq. (14) [namely $\zeta_H(t) < \zeta_{\text{CTH}}(t)$], an analogous procedure to identify parametric domains for the case in which the Hopf instability can only set in yields analogous information.

Based on Eq. (21), we can hence classify possible instability scenarios for our two-layer problem in a reduced parameter space (δ, B_0) as shown in Fig. 4(b), where, for simplicity, we consider the representative case $A_0 = 1$. The parameter space can be subdivided into three regions. In region I

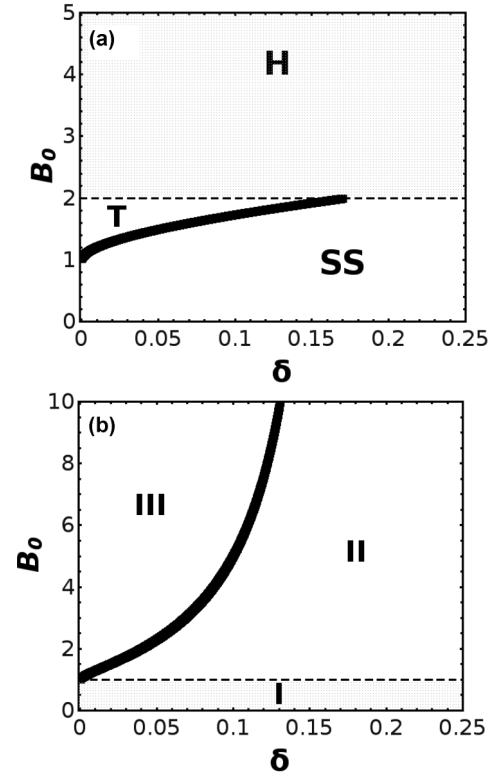


FIG. 4. Classification of the possible instabilities in the (δ, B_0) parameter space ($A_0 = 1$) for the system with (a) homogeneously distributed reactants and with (b) the two-layer configuration defined by Eqs. (2). The solid curve describes condition Eq. (21).

corresponding to all values of δ and $B_0 \leq 1$ no instability is expected and the system intermediates stabilize to nonzero steady states [scenario illustrated in Fig. 3(a)]. In region II a Hopf instability is the only one that can occur along the spatial domain and we can expect the formation of waves [scenario Fig. 3(b)]. The black curve describes Eq. (21), which delimits the lower borderline of region III where both Hopf and Turing instabilities can develop in space and time [scenario Fig. 3(c)]. Note that this curve tends to a vertical asymptote when $\delta \rightarrow (\sqrt{2} - 1)^2$, which is the corresponding Turing threshold for the analogous homogeneous system. In region III, we expect the emergence of localized stationary structures which can interact and eventually transmute into traveling structures around the CTH point.

IV. NONLINEAR SIMULATIONS

In order to validate the analytical approach above, we perform numerical simulations of the nonlinear Eqs. (3)–(6). The systems is solved by using the Crank-Nicolson method [52] over a one-dimensional spatial domain of length $L_\zeta = 500$, with a space integration step $h_\zeta = 0.5$. No-flux boundary conditions are imposed for the concentration fields at the boundaries of the reactor. Simulations are run for 5000 time units, using the integration time step $h_t = 1 \times 10^{-3}$. We set $A_0 = 1$, the diffusivities $D = D_x$ to 1 and $\delta = 0.1$, while we vary the relative amount of the initial reactant B_0 to explore changes in the spatiotemporal evolution of the system. To be

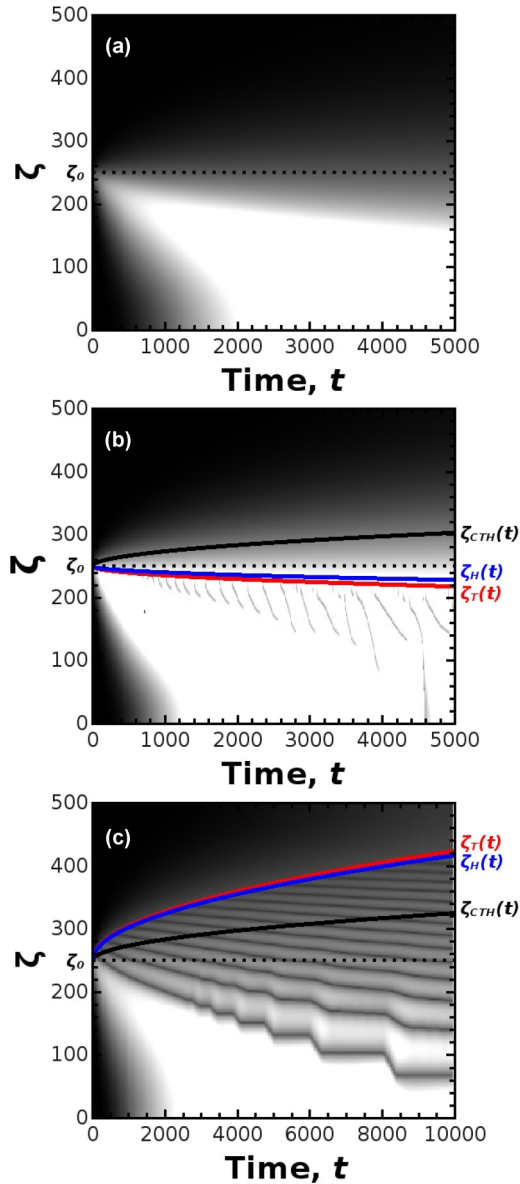


FIG. 5. Spatiotemporal dynamics of the inhibitor Y when $B_0 = 0.5$ (a), $B_0 = 2$ (b), and $B_0 = 15$ (c). Bright areas correspond to high concentration values of Y . Here $A_0 = 1$, $D = D_x = 1$, $\delta = 0.1$, and $k_a = k_b = 0$. The morphology of each space-time plot is correlated to the corresponding threshold curves $\zeta_{CTH}(t)$, $\zeta_H(t)$, and $\zeta_T(t)$.

more specific, we follow the transition from region I to III of the parameter space (δ, B_0) by varying B_0 with δ fixed to 0.1.

An overview of the main spatiotemporal dynamics observed is shown in Fig. 5. In each panel we report the space-time plots of the inhibitor Y , obtained by piling-up the spatial distribution of the concentration Y (vertical axis) as a function of time (horizontal axis). The spatiotemporal evolution of X is complementary to those shown. In order to correlate directly the morphology of the space-time plots with the spatiotemporal bifurcation diagrams described in Fig. 3, we overlap the corresponding threshold curves $\zeta_H(t)$, $\zeta_T(t)$, and $\zeta_{CTH}(t)$.

A common aspect characterizing the system dynamics in all the scenarios explored is that X rapidly stabilizes to the

steady-state $X = A_0$ over side 1 due to the first step of the kinetic model Eq. (1). Here, $Y \rightarrow 0$ because $B \rightarrow 0$ and it is autocatalytically depleted. The diffusion of the species X toward side 2 triggers the development of a diffusion-controlled front of the species Y regulated by the second and third kinetic steps of reaction scheme Eq. (1).

This phenomenology is typically illustrated by Fig. 5(a), where we show the space-time plot for $B_0 = 0.5$. We are then in case I and we can only observe the propagation of a diffusion-limited chemical front (bright area) from the initial contact point between the two reactant pools A and B toward side 2. As predicted in the classification drawn above, there is no location in space where $B(\zeta, t) > H(\zeta, t)$ or $T(\zeta, t)$ if $B_0 < 1$ and hence no corresponding breaks of symmetry take place.

Nevertheless, dynamical differences take place when B_0 is increased. Figure 5(b) displays the system dynamics when $B_0 = 2$ (case II). According to the parametric characterization of Fig. 4, in these conditions the system can locally undergo a Hopf instability that extends in the zone $\zeta < \zeta_H(t)$ [curve shown in blue in the space-time plot Fig. 5(b)]. The related dynamics exhibits the nucleation of waves effectively along $\zeta_H(t)$ and their development toward side 2. This area is increasingly refractory (high inhibitor concentration) downwards the spatial coordinate and the waves can only travel a short distance, vanishing before the bottom wall. This dynamics is reminiscent of tracking waves [53] found in the 1,4-cyclohexanedione Belousov-Zhabotinsky medium. Also, due to the spatial localization of the domain where waves can propagate and to the no-flux boundary conditions at the borders of the reactor, new waves are forced to interact with previous waves. As a result the spatiotemporal plots become progressively more complex, showing aperiodic dynamics across the $\zeta_H(t)$ threshold. Similar patterns (not shown) characterize the system dynamics within region II for larger values of δ .

The third case considered in Fig. 5(c), for $B_0 = 15$, illustrates the spatiotemporal dynamics when the Hopf and Turing regimes can coexist and intersect along the spatial domain. This corresponds to region III of the diagram in Fig. 4(b). From the phenomenological viewpoint, we can appreciate how stationary structures form on side 1, where the Turing instability can locally induce a breaking of symmetry. In agreement with analytical calculations, these transient stationary structures form in the region $\zeta_{CTH}(t) < \zeta < \zeta_T(t)$, confined between the red and the black curves in the space-time plot of Fig. 5(c). A further increment in B_0 has the effect of extending this Turing domain. In time, the stationary patterns forming in the Turing domain present an oscillatory amplitude (not visible in the space-time plot) and experience a drifting towards side 2 as soon as they approach the CTH point. While feeling the influence of the Hopf instability [i.e., for $\zeta < \zeta_H(t)$], these structures undergo intermittent pulsations reflecting the local frequency of the chemical oscillator. This, in turn, depends upon the local concentration of A : the lower the A concentration the lower the oscillation frequency. As a result, the waves progressively develop as a sort of wave packet showing aperiodic and increasingly delayed accelerations as the leading waves approach the lateral border of side 2, where the concentration of A is the lowest in the reactor. This phenomenology gives rise to characteristic zigzag

spatiotemporal patterns and features a genuine manifestation of the Turing-Hopf interaction.

Note that, in all the described scenarios, we have focused on the initial transient of the dynamics. In the long-term limit, where the concentration profiles A and B homogenize to the asymptotic values $A_0/2$ and $B_0/2$, the global dynamics of the system obeys the standard instability conditions of the homogeneous Brusselator as mentioned in Sec. II. However, our far-from-equilibrium assumptions then do not hold any longer and lead to physically meaningless results.

The validity of the pool chemical approximation used in the analytical calculations is tested by comparing the dynamics

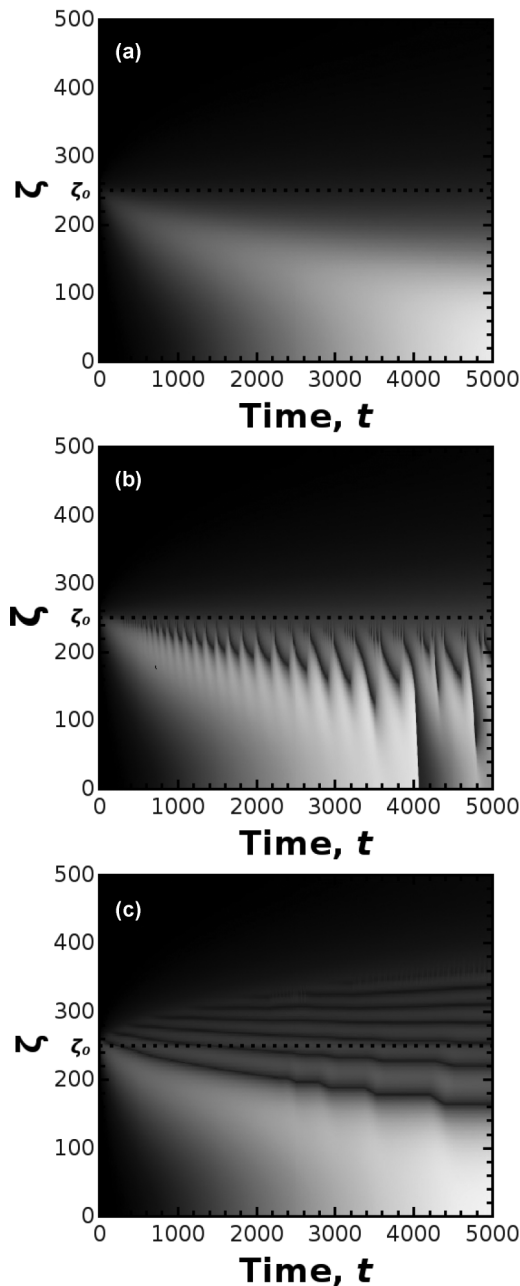


FIG. 6. Spatiotemporal dynamics of the inhibitor Y obtained with the same parameter setting as described in the caption of Fig. 5 [$B_0 = 0.5$ (a), $B_0 = 2$ (b), and $B_0 = 15$ (c)], but $k_a = k_b = 0.0001$.

obtained when the reactant consumption is neglected [i.e., with $k_a = k_b = 0$ in Eqs. (3) and (4); Fig. 5] with analogous simulations performed with increasing values of k_a and k_b (Fig. 6). Comparing Figs. 5 and 6, we can appreciate how similar spatiotemporal dynamics develop for $k_a = k_b < 0.0005$, while for larger values of these parameters, the depletion of the main reactants critically impacts the dynamics and, after a short transient, chemical species monotonically evolve towards the final stationary states.

V. CONCLUDING DISCUSSION

The spatial deployment of waves and of stationary Turing structures has been investigated theoretically when two regions containing the main reactants A and B , initially separated in space, are put in contact and a RD dynamics fueled by an $A + B \rightarrow$ oscillator reaction takes place around the contact zone. This two-layer configuration allows us to localize different instability zones over the spatial domain of the system. Using the Brusselator model, we have derived analytically the conditions for localization and interaction in space and time of Turing and Hopf modes in the parameter space of the problem spanned by the ratio δ of the intermediate species diffusion coefficients and the initial value B_0 of the bifurcation concentration $B(\zeta, t)$. We found that only two scenarios are possible: (i) localized Hopf-controlled spatial domains and (ii) coexisting and spatially adjacent Hopf and Turing regimes. Our approach to predict these conditions relies on the extension of the stability analysis valid for the homogeneous system (i.e., where the reactants are constant in space and time) to our space-time-dependent problem in which the reactants are initially spatially separated. Though simple, this strategy allows us to classify in the parameter space (δ, B_0) which instabilities are to be expected and to predict analytically the spatiotemporal deployment of these instability domains. While our theoretical approach gives quantitative constraints for instability scenarios, it can only provide qualitative insights on the characteristics of the resulting patterns. A more rigorous study could be developed via a linear stability analysis of Eqs. (5) and (6) by including the space-dependent distribution of the main reactants and their consumption in Eqs. (3) and (4), as proposed in Refs. [10,19,20]. In principle, by means of such methods it is possible to get the wavelength of stationary structures around the reactive zone and the oscillation frequency in the localized Hopf domain. However, given the nonstationarity of the problem presented here (the two main reactant concentrations change in space and time), these characteristics also depend on space and time, making our case more complicated. Also, the confinement of the dynamics imposed by no-flux boundary conditions (differently from the infinite spatial domain considered in typical analytical approaches) confers further complexity. In order to tackle this problem, we have thus performed direct nonlinear simulations to study the dynamics as a function of B_0 with δ fixed. Numerical results confirm the reliability of our theoretical framework and related analytical outcomes. In detail, we observe simple diffusion-limited chemical fronts when no instability can set in. By contrast, traveling waves emerge and move confined within a specific spatial region when the system is locally unstable toward a Hopf instability. Finally,

stationary structures can form locally and evolve in time into dynamical structures if both the Turing and the Hopf domains can coexist in the spatial domain. The interaction between the two instabilities is found to be at the basis of spatiotemporal *zigzag* waves.

To check to which extent our analytical results based on the pool chemical approximation are valid, we have also run numerical simulations of the model including (i) A and B consumption and backward reactions [30], or (ii) main reactant constant inflow at the lateral borders of the reactor. In this paper, we reported a comparison of the scenarios obtained with and without reactant consumption. As expected, we observed that analogous spatiotemporal instabilities as predicted by means of the analytical procedure can emerge when the reactants are slowly depleted, while no dissipative structures have a chance to form if A and B are consumed too fast and the system monotonically decays to the equilibrium.

To conclude, this work complements previous studies on pattern formation across the interface between two pools

of reactants and aims at extending the wide literature of the classical $A + B \rightarrow C$ problem to $A + B \rightarrow$ autocatalytic and oscillatory kinetics. Given the rich spectrum of possible reactant composition by which a two-layer configuration can be realized and the variety of possible different regimes, the present study paves the way to further experimental (for instance with BZ-microemulsions [54]) and theoretical investigations on this new class of systems. Also, the exploration and the classification of possible reaction-diffusion dynamics in two-layer systems feature the fundamental building block to understand complex interfacial pattern formation where hydrodynamic contributions are also at play and which are currently of utmost interest.

ACKNOWLEDGMENTS

We thank P. Borckmans for discussions and for a critical reading of the manuscript. We gratefully acknowledge funding by Prodex and PDR-FNRS FORECAST Projects.

-
- [1] L. Gálfi and Z. Rácz, *Phys. Rev. A* **38**, 3151 (1988).
 [2] Z. Jiang and C. Ebner, *Phys. Rev. A* **42**, 7483 (1990).
 [3] C. Almarcha, P. M. J. Trevelyan, P. Grosfils, and A. De Wit, *Phys. Rev. Lett.* **104**, 044501 (2010).
 [4] L. Lemaigre, M. A. Budroni, L. A. Riolfo, P. Grosfils, and A. De Wit, *Phys. Fluids* **25**, 014103 (2013).
 [5] T. Gérard and A. De Wit, *Phys. Rev. E* **79**, 016308 (2009).
 [6] L. A. Riolfo, Y. Nagatsu, S. Iwata, R. Maes, P. M. J. Trevelyan, and A. De Wit, *Phys. Rev. E* **85**, 015304 (2012).
 [7] D. M. Escala, M. A. Budroni, J. Carballido-Landeira, A. De Wit, and A. P. Muñozuri, *J. Phys. Chem. Lett.* **5**, 413 (2014).
 [8] B. P. Belousov, in *Sbornik Referatov po Radiatsionno Meditsine* (Medgiz, Moscow, 1958), p. 145.
 [9] A. N. Zaikin and A. M. Zhabotinsky, *Nature* **225**, 535 (1970).
 [10] M. Herschkowitz-Kaufman and G. Nicolis, *J. Chem. Phys.* **56**, 1890 (1972).
 [11] G. Nicolis and I. Prigogine, *Self-Organization in Nonequilibrium Systems* (Wiley, New York, 1977).
 [12] Z. Noszticzius, W. Horsthemke, W. D. McCormick, H. Swinney, and W. Y. Tam, *Nature* **329**, 619 (1987).
 [13] E. Dulos, J. Boissonade, and P. De Kepper, *Physica A* **188**, 120 (1992).
 [14] V. Castets, E. Dulos, J. Boissonade, and P. De Kepper, *Phys. Rev. Lett.* **64**, 2953 (1990).
 [15] P. De Kepper, E. Dulos, J. Boissonade, A. De Wit, G. Dewel, and P. Borckmans, *J. Stat. Phys.* **101**, 495 (2000).
 [16] I. Lengyel, S. Kádár, and I. R. Epstein, *Phys. Rev. Lett.* **69**, 2729 (1992).
 [17] G. Dewel, P. Borckmans, A. De Wit, B. Rudovics, J.-J. Perraud, E. Dulos, J. Boissonade, and P. De Kepper, *Physica A* **213**, 181 (1995).
 [18] S. Setayeshgar and M. C. Cross, *Phys. Rev. E* **58**, 4485 (1998).
 [19] G. Dewel and P. Borckmans, *Phys. Lett. A* **138**, 189 (1989).
 [20] G. Dewel and P. Borckmans, in *Patterns, Defects and Materials Instabilities*, edited by D. Walgraef and N. M. Ghoniem (Kluwer Academic Publishers, Dordrecht/Boston/London, 1989), p. 63.
 [21] J. Boissonade, *J. Phys. France* **49**, 541 (1988).
 [22] J. Brindley, C. Kaas-Petersen, J. H. Merkin, and S. K. Scott, *Phys. Lett. A* **128**, 260 (1988).
 [23] P. Borckmans, A. De Wit, and G. Dewel, *Physica A* **188**, 137 (1992).
 [24] A. De Wit, *Adv. Chem. Phys.* **109**, 435 (1999).
 [25] O. Jensen, V. O. Pannbacker, E. Mosekilde, G. Dewel, and P. Borckmans, *Phys. Rev. E* **50**, 736 (1994).
 [26] L. Yang, M. Dolnik, A. M. Zhabotinsky, and I. R. Epstein, *J. Chem. Phys.* **117**, 7259 (2002).
 [27] V. K. Vanag and I. R. Epstein, *Phys. Rev. Lett.* **90**, 098301 (2003).
 [28] V. K. Vanag and I. R. Epstein, *Phys. Rev. Lett.* **92**, 128301 (2004).
 [29] I. Prigogine and R. Lefever, *J. Chem. Phys.* **48**, 1695 (1968).
 [30] R. Lefever, G. Nicolis, and P. Borckmans, *J. Chem. Soc., Faraday Trans. 1* **84**, 1013 (1988).
 [31] J.-J. Perraud, A. De Wit, E. Dulos, P. De Kepper, G. Dewel, and P. Borckmans, *Phys. Rev. Lett.* **71**, 1272 (1993).
 [32] P. Borckmans, G. Dewel, A. De Wit, and D. Walgraef, in *Chemical Waves and Patterns*, edited by R. Kapral and K. Showalter (Kluwer, Dordrecht, The Netherlands, 1995), p. 323.
 [33] A. De Wit, D. Lima, G. Dewel, and P. Borckmans, *Phys. Rev. E* **54**, 261 (1996).
 [34] M. Meixner, A. De Wit, S. Bose, and E. Schöll, *Phys. Rev. E* **55**, 6690 (1997).
 [35] W. Just, M. Bose, S. Bose, H. Engel, and E. Schöll, *Phys. Rev. E* **64**, 026219 (2001).
 [36] D. G. Míguez, S. Alonso, A. P. Muñozuri, and F. Sagués, *Phys. Rev. Lett.* **97**, 178301 (2006).
 [37] A. Bhattacharyay, *J. Phys. A: Math. Gen.* **39**, 8557 (2006).
 [38] J. C. Tzou, A. Bayliss, B. J. Matkowsky, and V. A. Volpert, *Math. Model. Nat. Phenom.* **6**, 87 (2011).
 [39] J. C. Tzou, Y.-P. Ma, A. Bayliss, B. J. Matkowsky, and V. A. Volpert, *Phys. Rev. E* **87**, 022908 (2013).
 [40] A. De Wit, G. Dewel, and P. Borckmans, *Phys. Rev. E* **48**, R4191 (1993).

- [41] S. Bouzat and H. S. Wio, *Phys. Lett. A* **268**, 323 (2000).
- [42] G. Gambino, M. Lombardo, and M. Sammartino, *Math. Comput. Simul.* **82**, 1112 (2012).
- [43] V. K. Vanag and I. R. Epstein, *Phys. Chem. Chem. Phys.* **11**, 897 (2009).
- [44] M. A. Budroni and F. Rossi, *J. Phys. Chem. C* **119**, 9411 (2015).
- [45] M. A. Budroni, L. Lemaigre, A. De Wit, and F. Rossi, *Phys. Chem. Chem. Phys.* **17**, 1593 (2015).
- [46] M. A. Budroni, *Phys. Rev. E* **92**, 063007 (2015).
- [47] M. A. Budroni, L. Lemaigre, D. M. Escala, A. P. Muñuzuri, and A. De Wit, *J. Phys. Chem. A* **120**, 851 (2016).
- [48] V. K. Vanag and I. R. Epstein, *J. Phys. Chem. A* **106**, 11394 (2002).
- [49] T. Kolokolnikov, T. Erneux, and J. Wei, *Physica D: Nonlinear Phenomena* **214**, 63 (2006).
- [50] Scaled variables: $t = k_4 \tau$; $D_i = \tilde{D}_i / k_4$; $A = \sqrt{k_1^2 k_3 / k_4^3} [A]$; $B = (k_2 / k_4) [B]$; $X = \sqrt{k_3 / k_4} [X]$; $Y = \sqrt{k_3 / k_4} [Y]$; where τ , \tilde{D}_i , and $[I]$ are the dimensional time, diffusion coefficient, and concentration of species I , respectively.
- [51] J. Crank, *The Mathematics of Diffusion* (Clarendon Press, Oxford, 1975).
- [52] J. Crank and P. Nicolson, *Proc. Camb. Phil. Soc.* **43**, 50 (1947).
- [53] N. Manz, C. T. Hamik, and O. Steinbock, *Phys. Rev. Lett.* **92**, 248301 (2004).
- [54] V. K. Vanag and I. R. Epstein, *Phys. Rev. Lett.* **87**, 228301 (2001).